



Spin-wave excitations in the ferromagnetic metallic and in the charge-, orbital-, and spin-ordered states in $\text{Nd}_{1-x}\text{Sr}_x\text{MnO}_3$ with $x \approx 0.5$

H. Ulbrich,^{1,*} F. Krüger,^{2,†} A. A. Nugroho,³ D. Lamago,^{4,5} Y. Sidis,⁵ and M. Braden^{1,‡}

¹*II. Physikalisches Institut, Universität zu Köln, Zùlpicher Strasse 77, D-50937 Köln, Germany*

²*School of Physics & Astronomy, University of St. Andrews, North Haugh, St. Andrews, Fife KY16 9SS, United Kingdom*

³*Faculty of Mathematics and Natural Sciences, Institut Teknologi Bandung, Jl. Ganesha 10 Bandung, 40132 Indonesia*

⁴*Forschungszentrum Karlsruhe, Institut für Festkörperphysik, P.O.B. 3640, D-76021 Karlsruhe, Germany*

⁵*Laboratoire Léon Brillouin, C.E.A./C.N.R.S., F-91191 Gif-sur-Yvette Cedex, France*

(Received 28 July 2011; published 28 September 2011)

We report inelastic neutron-scattering experiments on single crystals of $\text{Nd}_{1-x}\text{Sr}_x\text{MnO}_3$ with $x = 0.5$ and $x = 0.49$. The spin-wave dispersion in the charge-, orbital-, and spin-ordered state in $\text{Nd}_{0.5}\text{Sr}_{0.5}\text{MnO}_3$ exhibits a strongly anisotropic stiffness. The sign of the anisotropy is characteristic for the site-centered model for charge and orbital ordering in half doped manganites. Within this model, linear spin-wave theory yields a perfect description of the experimental dispersion. In the ferromagnetic metallic state of $\text{Nd}_{1-x}\text{Sr}_x\text{MnO}_3$ with $x = 0.49$ and $x = 0.50$ magnetic excitations exhibit nearly the same magnon dispersion. High intense signals near the zone boundary over a wide energy level overlap with a sharp spin-wave dispersion, which can be described with a Heisenberg model including nearest-neighbor interactions.

DOI: [10.1103/PhysRevB.84.094453](https://doi.org/10.1103/PhysRevB.84.094453)

PACS number(s): 75.10.Hk, 75.25.Dk, 75.30.Ds

I. INTRODUCTION

In spite of its eminent relevance for colossal magnetoresistance (CMR) the exact nature of the charge-, orbital-, and spin-ordered (COSO) state in the manganites $R_{1-x}A_x\text{MnO}_3$ (R = rare earth, A = bivalent alkaline earth) with an antiferromagnetic insulating ground state is still under debate. The huge change in resistivity results from the competition between a ferromagnetic (FM) metallic and an antiferromagnetic (AFM) insulating state. A comprehensive understanding of the magnetic ordering is essential to get a wide understanding of CMR.

The parent compound LaMnO_3 with a transition-metal valence of Mn^{3+} exhibits a ground state which is characterized by an antiferromagnetic A -type ordering.^{1,2} The ratio of $\text{Mn}^{3+}:\text{Mn}^{4+}$ can be controlled by substitution of three-valent R with two-valent A leading to complex phase diagrams with a correlated charge-, orbital-, and spin-ordered ground state (see Ref. 3 for a brief summary). In spite of the numerous publications in perovskite (113) manganites around half doping, its COSO state has not been fully established.⁴⁻⁸ Some 113 manganites around $x = 0.5$ exhibit an A -type AFM metallic or FM metallic ground state while a decrease of the one-electron bandwidth leads to an AFM insulating state with CE-type ordering.⁵

The COSO state in half doped $\text{La}_{1-x}\text{Ca}_x\text{MnO}_3$ has been first studied by Wollan and Koehler and by Goodenough proposing a simple checkerboard ordering of Mn^{3+} and Mn^{4+} ions (Goodenough model).^{9,10} Additionally, the e_g orbitals on Mn^{3+} sites order in stripelike patterns and spins order in an antiferromagnetic alignment called CE type (see Fig. 1). The magnetic moments follow the orbital arrangement forming ferromagnetic zigzag chains while adjacent chains couple antiferromagnetically. First structural studies confirm the Goodenough model qualitatively, but the charge modulation appears to be significantly below the ideal value.^{4,11,12} Single-crystal neutron-diffraction experiments on $\text{Pr}_{0.6}\text{Ca}_{0.4}\text{MnO}_3$ are not in agreement with the site-centered charge-ordering picture but

propose charge order on the Mn-O-Mn bonds, forming Zener polarons (Zener-polaron model) yielding ferromagnetically coupled dimers.^{13,14} The nature of the COSO state is thus still a matter of debate and a clear proof for one of these models is still missing for $R_{1-x}A_x\text{MnO}_3$.

The magnetic exchange coupling follows the orbital occupations. Consequently a careful study of these interaction parameters by analyzing the spin-wave dispersion can give a direct view on the orbital arrangement. Indeed, for the single-layered (214) manganite $\text{La}_{0.5}\text{Sr}_{1.5}\text{MnO}_4$, inelastic neutron-scattering experiments established the spin-wave dispersion yielding strong support for the COSO state described qualitatively by the Goodenough model.¹⁵ In the magnetic ground state, acoustical branches exhibit a steep spin-wave dispersion parallel to the zigzag chains and a flatter dispersion perpendicular to them. These observations indicate a strong coupling inside the zigzag chains and a weak coupling between adjacent chains as it is expected for the Goodenough model. On the contrary, the Zener-polaron model implies a strong ferromagnetic coupling between the dimers and hence an anisotropy opposite to the observations.

Perovskite manganites exhibit intrinsic twinning rendering microscopic investigations quite complex. The high-temperature structural phase transition associated with a lowering of the symmetry from cubic down to orthorhombic results in six different domain orientations.¹⁶ The occurrence of charge and orbital order can only enhance the number of different domains. The magnetic neutron scattering at a magnetic superstructure reflection in a twinned crystal is thus reduced by roughly a factor of 6 compared to a monodomain crystal. The same holds for the inelastic signal arising from a low-energy magnon. The interpretation of inelastic neutron-scattering experiments is further aggravated by unavoidable superposition of the signals from different domain orientations at higher energy.

Due to the absence of twinning, the spin-wave dispersion and detailed studies in the COSO state has first been studied

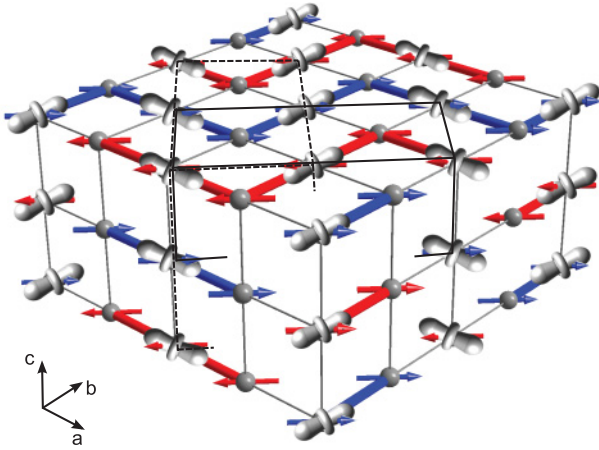


FIG. 1. (Color online) Schematic representation of a half doped perovskite manganite with charge, orbital, and antiferromagnetic CE-type ordering (Goodenough model). The pattern shows zigzag chains propagation in $[1,1,0]$ direction (cubic notation). The e_g orbital ordering on Mn^{3+} ions is shown by $d_{3x^2-r^2}$ and $d_{3y^2-r^2}$ orbitals. Mn^{4+} ions are drawn by balls while arrows stand for the magnetic alignment of the spins. The orbital unit cell is indicated by dashed black lines and the magnetic unit cell of Mn^{3+} by black dotted lines.

in single-layered manganites $\text{La}_{1-x}\text{Sr}_{1+x}\text{MnO}_4$.^{15,17–20} The e_g orbitals in the undoped compound LaSrMnO_4 are dominantly aligned perpendicular to the planes, but upon doping in $\text{La}_{1-x}\text{Sr}_{1+x}\text{MnO}_4$ these e_g orbitals flop into the MnO layers,¹⁸ so that the ground state of the 214 manganites around half doping qualitatively resembles that in 113 manganites at low temperatures.²¹ There is thus strong support that the qualitative CE model describes the ground state in single-layered half doped $\text{La}_{0.5}\text{Sr}_{1.5}\text{MnO}_4$. However, it remains an open issue whether the conventional AFM CE-type model may account for all COSO phases in manganites with $x \approx 0.5$, or whether the order essentially changes with the dimensionality (three-dimensional versus two-dimensional materials) and with the structural distortions associated with the buckling of the MnO layers. Furthermore, in spite of its charge- and orbital-ordered ground state, single-layered manganites exhibit no CMR under moderate magnetic field most likely due to the enhanced stability of the COSO state in layered materials.²² Consequently, it is a matter of particular interest to extend the study of the spin-wave dispersion in the COSO state to perovskite manganites. There is a tremendous number of publications on magnetic excitations in the ferromagnetic metallic phase and in the A-type AFM phase in perovskite manganites.^{5,23–31} But to the best of our knowledge, investigations of the spin-wave dispersion in 113 manganites in the COSO state with AFM CE-type ordering are still missing. A microscopic analysis of both the ferromagnetic metallic and the antiferromagnetic insulating state is important to understand the switching between these phases by external parameters like pressure, magnetic field, or temperature.

In the paper we present experimental and theoretical analysis of the spin-wave dispersion in $\text{Nd}_{1-x}\text{Sr}_x\text{MnO}_3$ with $x = 0.50$ and $x = 0.49$. Antiferromagnetic CE-type ordering

in $\text{Nd}_{1-x}\text{Sr}_x\text{MnO}_3$ has been shown to occur only in a very small doping range near $x = 0.5$.^{8,32,33} A slight change of stoichiometry from $x = 0.50$ to $x = 0.49$ can lead to a ground state in which ferromagnetic ordering and antiferromagnetic CE-type order coexist, while the ferromagnetic metallic (FMM) state above the COSO state is stable in a broader concentration range.³² The paper is divided as follows: After the experimental section we start by discussing the COSO state of the half doped compound $\text{Nd}_{0.5}\text{Sr}_{0.5}\text{MnO}_3$. We present experimental data of the spin-wave dispersion up to energies of about 12 meV and compare these results with linear spin-wave theory. In the second part we present inelastic-scattering measurements in the FMM state of $\text{Nd}_{0.5}\text{Sr}_{0.5}\text{MnO}_3$ and of $\text{Nd}_{0.51}\text{Sr}_{0.49}\text{MnO}_3$ along the main-symmetry directions and give a description of the FM magnon dispersion by a simple Heisenberg model.

II. EXPERIMENT

Two large single crystals of $\text{Nd}_{1-x}\text{Sr}_x\text{MnO}_3$ with $x = 0.49$ and $x = 0.50$ have been grown by the floating-zone method. The starting materials, Nd_2O_3 , SrCO_3 , and MnO_2 , were preheated and mixed in appropriate stoichiometric proportions. After sintering for several times at 1000°C and 1200°C a cylindrical rod with 90 mm length and 10 mm diameter was pressed and heated at 1500°C . The apparatus used for crystal growth was the floating-zone furnace (Crystal Systems Incorporated), equipped with four halogen lamps. The feed and seed rods were rotated in opposite directions at about 15 rpm. The molten zone was vertically moved at a rate of 2–3 mm/h in a pressure of pure oxygen atmosphere (2 bars). The high quality of the two samples has been checked by macroscopic and microscopic studies. Magnetization was measured by a superconducting quantum interference device (SQUID) magnetometer, electric resistivity by a standard four-contact method, and x-ray powder-diffraction experiments were carried out on a D5000 Siemens diffractometer.

$\text{Nd}_{1-x}\text{Sr}_x\text{MnO}_3$ with $x = 0.49$ and $x = 0.50$ crystallizes in the orthorhombic unit cell with space group $Ibmm$ and room-temperature lattice parameters of $a \approx \sqrt{2} \times a_p$, $b \approx \sqrt{2} \times a_p$, $c \approx 2 \times a_p$, where a_p is the lattice parameter of the cubic perovskite. In the following we use the cubic notations with $a_p = 3.84 \text{ \AA}$ and hence the reciprocal-lattice vectors are given in reduced lattice units as $\mathbf{Q} = (h, k, l) = \frac{2\pi}{a_p}(q_x, q_y, q_z)$. $\text{Nd}_{1-x}\text{Sr}_x\text{MnO}_3$ with $x = 0.49$ and $x = 0.50$ is a paramagnetic-insulator at room temperature and undergoes a transition into a FMM ordered state below $T_C \approx 250 \text{ K}$. Upon cooling a transition of first order from the FMM state into a correlated charge-, orbital-, and antiferromagnetic spin-ordered state can be observed.^{32,34,35}

All of our neutron-scattering experiments have been performed at the Laboratoire Léon Brillouin in Saclay. Diffraction experiments were made using the 3T.1 diffractometer and the G4.3 spectrometer. Inelastic neutron data were collected with the 1T and 4F.2 spectrometers. The spectrometer 1T, installed on the thermal channel of the reactor, was used with a pyrolytic graphite (PG) monochromator and with a PG analyzer. To suppress higher harmonics two PG filters were installed and the final neutron energy was fixed at either $E_f = 14.7 \text{ meV}$

or $E_f = 8.04$ meV. The cold three-axis spectrometer 4F.2 working with a PG double monochromator was used with a Be filter to suppress higher harmonics.

III. CHARGE-, ORBITAL-, AND SPIN-ORDERED STATE IN $\text{Nd}_{0.5}\text{Sr}_{0.5}\text{MnO}_3$

The ferromagnetic metallic and antiferromagnetic insulating states in our single crystal of $\text{Nd}_{0.5}\text{Sr}_{0.5}\text{MnO}_3$ have been well characterized by macroscopic techniques and by diffraction experiments demonstrating the high quality of our sample. Measurements of electric resistivity as a function of temperature indicate a transition into a (half) metallic state below $T_C = 255$ K and simultaneously a rapid increase of magnetization points to ferromagnetic ordering [Figs. 2(a) and 2(d)]. The transition into a charge-, orbital-, and spin-ordered state at $T_{CO} \approx 160$ K is of the first order. Hereby, the electrical resistivity exhibits a jump by more than three orders of magnitude and the magnetization vanishes. X-ray powder diffraction has been performed from $T = 15$ K up to $T = 850$ K. The refinement of the data was carried out with the Rietveld method implemented in the FULLPROF suite.³⁶ The best description of the data can be obtained with the

space group $Ibmm$ for the studied temperature range. The symmetry reduction from the space group $Pm\bar{3}m$ of an ideal undistorted perovskite to space group $Ibmm$ arises from tilting of MnO_6 octahedra around an axis parallel to the edges in the ab planes. The orthorhombic distortion of the lattice parameters increases rapidly at $T = 550$ K, which can arise from an orbital ordering effect of Mn^{3+} ions [Fig. 2(c)]. Upon cooling through the FMM phase transition, a slight increase of the orthorhombic c axis with a shrinking of the a and b axis is observed. It appears likely that upon entering the FMM state an enhancement of the in-plane metallicity in an FM exchange is favored. An abrupt change of the lattice parameters during the transition into the COSO state indicates a sudden and strong structural change [Fig. 2(b)]. Temperature-dependent neutron-diffraction experiments at the Bragg reflection $\mathbf{Q}_{FM} = (1,0,0)$ prove ferromagnetic ordering between $T_{CO} < T < T_C$, which is in perfect agreement with our magnetization data [Fig. 2(e)]. Note that the FM signal at $\mathbf{Q}_{FM} = (1,0,0)$ is also visible above T_C , but it gets strongly suppressed in the COSO state. The temperature-dependent behavior of the superstructure reflection intensity of $\mathbf{Q}_{Mn^{3+}} = (0.25, 0.25, 0.5)$ provides information on magnetic ordering of Mn^{3+} below T_{CO} [Fig. 2(e)]; for more details see Ref. 19.

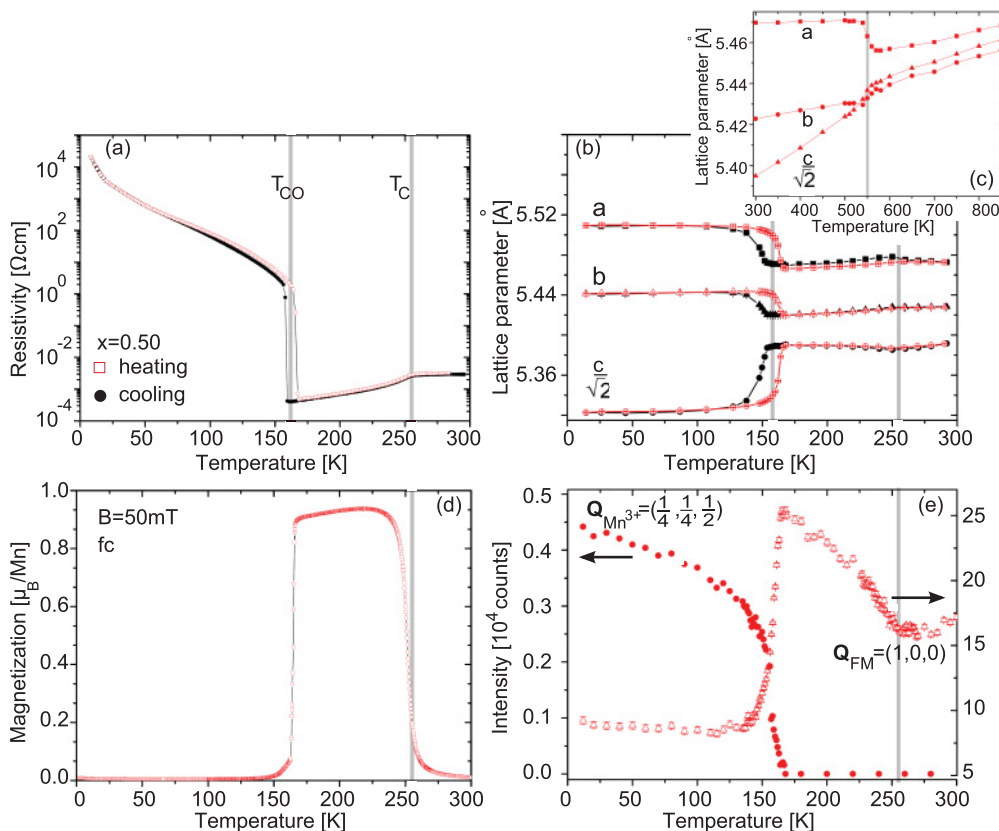


FIG. 2. (Color online) Temperature dependence of transport measurements and structural investigations of $\text{Nd}_{0.5}\text{Sr}_{0.5}\text{MnO}_3$. Experimental data of electric resistivity upon cooling show a kink at the transition into the (half) metallic state at $T_C = 255$ K (a), and the occurrence of the COSO state at $T_{CO} \approx 160$ K causes a sudden jump in resistivity by three orders of magnitude pointing to insulating behavior. Magnetization data indicating a ferromagnetically ordered state below T_C and an antiferromagnetically ordered state below T_{CO} (d). X-ray powder diffraction from $T = 15$ K up to $T = 850$ K shows remarkable changes of the orthorhombic structure at various temperatures in accordance with electric and magnetic properties (b),(c). Neutron diffraction at the superstructure reflection $\mathbf{Q}_{FM} = (1,0,0)$ indicates ferromagnetic ordering between $T_{CO} < T < T_C$. Furthermore, superstructure reflections referring to antiferromagnetic ordering of Mn^{3+} can be detected below T_{CO} (e). For more details see text.

The quality of our sample is evident from the observed sharp transitions, the increase in resistivity by several orders of magnitude, and from the perfect agreements of T_C and T_{CO} with published data.^{34,35} Although charge and orbital ordering cannot be directly detected by neutron diffraction, charge and orbital ordering leads to a characteristic distortion of the MnO_6 octahedra that are visible in neutron-diffraction experiments due to the higher sensitivity to oxygen.

The Goodenough model predicts an alternating charge ordering of Mn^{3+} and Mn^{4+} ions. Considering an initially ideal cubic perovskite, this doubles the structural unit cell to $(\sqrt{2}a_p \times \sqrt{2}a_p \times a_p)$ and causes superstructure reflections with propagation vector $\mathbf{k}_{co} = (\pm\frac{1}{2}, \pm\frac{1}{2}, 0)$. Crystallographic studies find far smaller disproportion than a complete $\text{Mn}^{3+}/\text{Mn}^{4+}$ (see Refs. 11 and 12). Nevertheless, we use the nominal labels Mn^{3+} and Mn^{4+} throughout this paper. The orbital ordering of e_g electrons on Mn^{3+} sites reduces the symmetry to orthorhombic with lattice parameters $2\sqrt{2}a_p$ along $[1,1,0]$ and $\sqrt{2}a_p$ along $[-1,1,0]$ for zigzag chains running along $[1,1,0]$. As the zigzag chains can propagate along $[1,1,0]$ and $[-1,1,0]$, orbital superstructure reflections with propagation vector $\mathbf{k}_{oo} = (\pm\frac{1}{4}, \pm\frac{1}{4}, 0)$ can be detected. The orthorhombic distortion induces a twofold twinning since the orbitals can stack either along the $[1,1,0]$ or $[-1,1,0]$ direction. Both arrangements superimpose and contribute to an equal amount in the scattering geometry studied in our sample. The superposition with the structural twinning in these pseudocubic compounds can lead to a very complex twinned structure in the COSO state. The charge and orbital ordering implies an antiferromagnetic CE-type ordering with ferromagnetic alignment of magnetic moments along the chains and antiferromagnetic coupling of adjacent chains. Figure 1 shows a schematic representation of the charge, orbital, and spin ordering with zigzag chains propagation in the $[1,1,0]$ direction. In perovskite manganites the planes of the orbital ordering always align with the structural distortions

due to the octahedron tilting. The latter leads to a unit cell $\sqrt{2}a_p \times \sqrt{2}a_p \times 2a_p$ with the doubling being always perpendicular to the layers of orbital order (note that the zigzag chains run in these). Due to the strong structural distortion, orbitals and charges align in rows along this perpendicular direction (c axis). Charge and orbital order are thus not modulated along this direction, corresponding to a ferro-type stacking. In the following the stacking direction is taken always along $[0,0,1]$ in our cubic notation.³⁷ The magnetic CE-type spin ordering results in two sublattices: the magnetic unit cell of Mn^{4+} and the magnetic sublattice of Mn^{3+} . The latter one is depicted in Fig. 1. Superstructure reflections referring to the spin ordering of Mn^{4+} can be detected at propagation vectors $\mathbf{k}_{\text{Mn}^{4+}} = \pm(\frac{1}{2}, 0, \frac{1}{2})$ or $\mathbf{k}_{\text{Mn}^{4+}} = \pm(0, \frac{1}{2}, \frac{1}{2})$ and superstructure reflections referring to magnetic ordering of Mn^{3+} at $\mathbf{k}_{\text{Mn}^{3+}} = \pm(\frac{1}{4}, \pm\frac{1}{4}, \frac{1}{2})$. To investigate pure charge or orbital ordering we have to measure superstructure reflections with large Q where magnetic order is negligible because the magnetic form factor decreases rapidly with increasing scattering vector.

To study the spin-wave dispersion in the AFM ordered state along the main-symmetry directions, we aligned the sample in two different scattering planes. Most of our experiments have been done by aligning the crystal in the $(1,1,0)/(0,0,1)$ scattering plane to access momentum transfers of the kind (h,h,l) . In order to focus on the spin-wave dispersion parallel to the zigzag chains the sample was orientated in a less conventional geometry with reflections $(2,1,1)/(0,1,-1)$ defining the scattering plane. The spin-wave dispersion at $T = 12$ K, observed by inelastic neutron scattering from 2 meV up to about 12 meV, is depicted in Fig. 3. The solid lines correspond to a fit based on linear spin-wave theory. Details on the theoretical calculations of the magnetic excitation spectrum are given below. Besides the superposition of all twins rendering the study at high energies impossible, we observe Q -independent signals around 0.9 meV and around 12 meV pointing to crystalline electric field (CEF) excitations

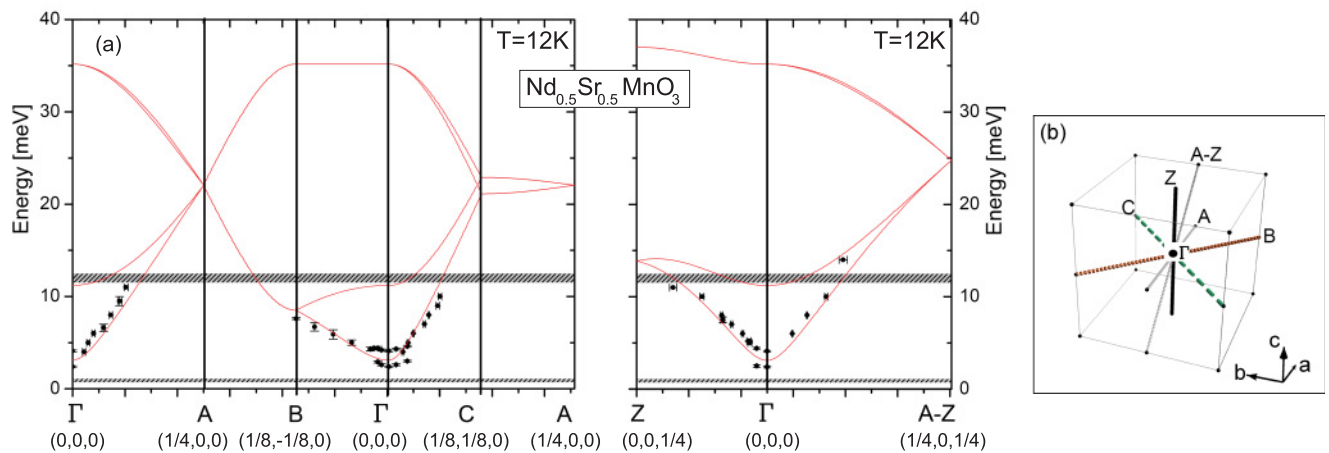


FIG. 3. (Color online) Dispersion of the magnetic excitations in $\text{Nd}_{0.5}\text{Sr}_{0.5}\text{MnO}_3$ along the main-symmetry directions (a). The path Γ -A stands for investigations in $[1,0,0]$ direction (diagonal to the chains), while Γ -B measures the dispersion perpendicular and Γ -C parallel to the zigzag chains. Investigations parallel to the c axis are presented by Γ -Z. Solid curves are fits as described in the text and crystal-field excitations of the Nd ions are indicated by gray-shaded bars. The different paths along the main-symmetry directions around an antiferromagnetic zone center for chains propagation in $[1,1,0]$ directions is shown in (b).

of the Nd ions. Scans in different Brillouin zones and observations in similar compounds support this conclusion.^{28,38,39} Consequently clear magnetic excitations in all symmetry directions at 12 meV are not recordable. Our spin-wave studies have been performed around several antiferromagnetic zone centers, $\Gamma = (\frac{h}{4}, \frac{k}{4}, \pm \frac{1}{2})$ with h, k odd integer, and have been combined to the presented dispersion. Figure 4 shows examples of typical raw-data scans to study the spin-wave dispersion along the main-symmetry directions. We were able to separate between different paths since only one of the orbital twins contributes to a quarter-indexed magnetic zone center. For example, to measure the spin-wave perpendicular to the zigzag chains (Γ - B) starting at the zone center $(\frac{1}{4}, \frac{3}{4}, \frac{1}{2})$ one has to measure along the $[-1, 1, 0]$ direction while the $[1, 1, 0]$ direction measures the path parallel to the zigzag chains (Γ - C) [Fig. 3(b)]. Starting from the antiferromagnetic zone center, we find a gap and a splitting into two single modes, similar to observations in the single-layered system $\text{La}_{0.5}\text{Sr}_{1.5}\text{MnO}_4$.¹⁵ The degeneracy of the two AFM magnon branches seems to be removed due to the single-ion anisotropy. Energy scans at several magnetic zone centers exhibit two well distinguishable contributions at energies $E_1 = 2.4(1)$ meV and $E_2 = 4.1(1)$ meV [Fig. 5(a)]. The gap and energy splitting of the lowest excitations can be explained by the alignment of the magnetic moments. The easy axis of the magnetic moments of $\text{Nd}_{0.5}\text{Sr}_{0.5}\text{MnO}_3$ is in the ab plane at an angle of 45° with respect to the a and b axes (cubic notations).³² To study the splitting near the zone center and to follow the two modes in the Γ - B and Γ - C directions we performed inelastic neutron

experiments with the cold-source spectrometer. Away from the zone center, at $q > 0.025$, the two excitations merge into a single signal.

The lowest acoustic branch along the Γ - C path exhibits a steeper dispersion than that along the Γ - B path. The end point of the acoustic branch at B can be observed at $7.5(1)$ meV. At this energy, we find the acoustic branch along Γ - C in the middle of the Brillouin zone pointing to a stronger ferromagnetic coupling parallel to the zigzag chains in comparison to the coupling perpendicular to the chains. Although magnetic excitations at the zone boundary parallel to the chains can experimentally not be resolved due to the twinning, the anisotropic behavior is apparent. Our theoretical calculations predict a magnon energy of about 22 meV at the zone boundary, which is three times larger than the end point B of the Γ - B branch. This study is in full agreement with the observations in $\text{La}_{0.5}\text{Sr}_{1.5}\text{MnO}_4$.¹⁵ The antiferromagnetic coupling along the c direction (Γ - Z) exhibits an intermediate dispersion: this means a steeper acoustic branch in comparison to the antiferromagnetic coupling in Γ - B , but flatter than the ferromagnetic coupling along the zigzag chains (Γ - C). Consequently the antiferromagnetic coupling between adjacent chains is weaker in comparison to the antiferromagnetic stacking in the c direction. This is fundamentally different in the layered materials, where there is no significant c -axis coupling. The CE-type order in $\text{Nd}_{0.5}\text{Sr}_{0.5}\text{MnO}_3$ is thus, as expected, much more three-dimensional in nature, the AFM stacking in the c direction is stronger than the AFM coupling between zigzag chains in the ab layers.

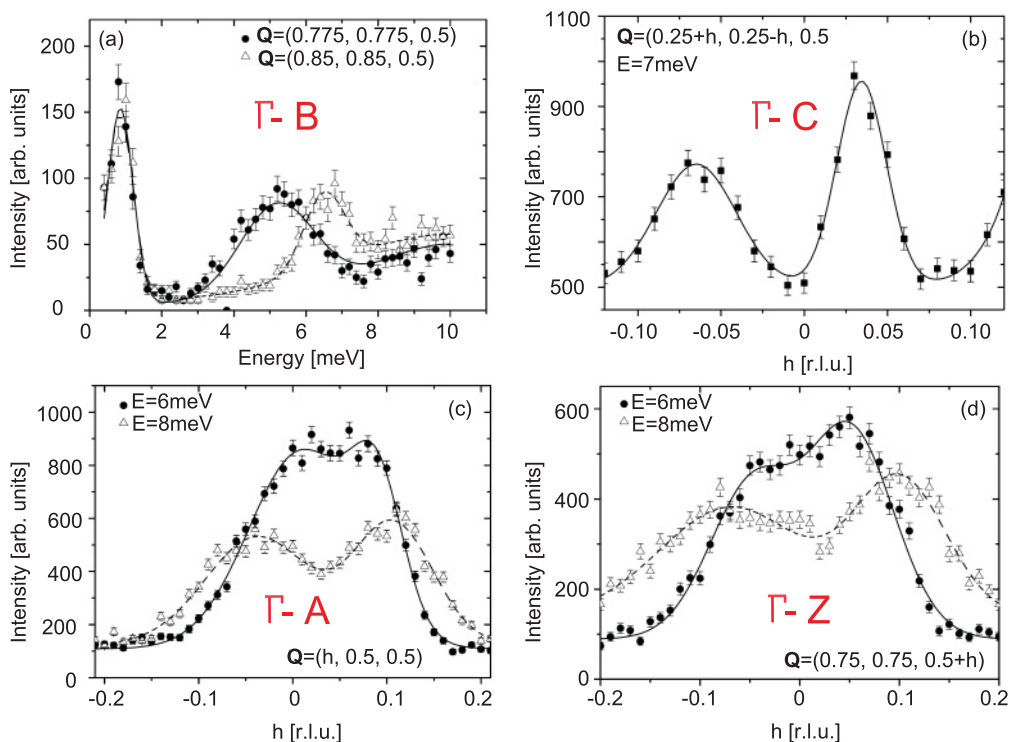


FIG. 4. (Color online) Representative energy and constant-energy scans at $T = 12$ K in $\text{Nd}_{0.5}\text{Sr}_{0.5}\text{MnO}_3$ along the main-symmetry directions. Two constant- Q scans that measures the dispersion along Γ - B are depicted in (a). Constant-energy scans to study the acoustic branch parallel to the chains (Γ - C), 45° diagonal to the chains (Γ - A), and in the c direction (Γ - Z) are shown in (b) and (c). Solid lines correspond to fits with Gaussians.

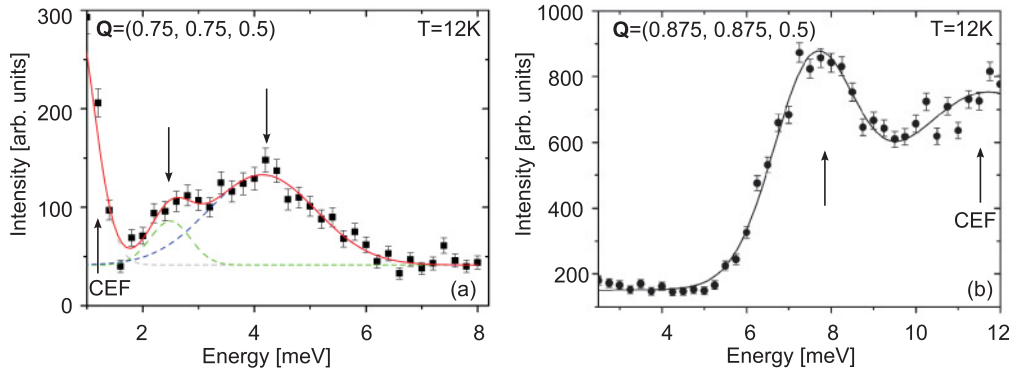


FIG. 5. (Color online) Energy scans in the first Brillouin zone at the antiferromagnetic center $\mathbf{Q} = (0.75, 0.75, 0.5)$ (a) and at the zone boundary B along the acoustic branch Γ - B (b). The gap and the splitting of the excitations at the zone center is clearly observable (indicated by black arrows). The signal around $E = 1$ meV corresponds to CEF excitations of the Nd ions. (The elastic line is not shown.) The excitation at the end point B can be observed at 7.5(1) meV while the signal around 12 meV can be ascribed to a CEF as well (b). Dashed lines correspond to individual fits with Gaussians and the solid line to the resulting fit.

Theoretically, the formation of the CE-type superstructure close to half filling is understood in terms of the degenerate double-exchange (DDEX) model.^{6,14,40,41} The t_{2g} electrons form local magnetic moments (core spins), which are coupled to the itinerant electrons of the degenerate e_g orbitals by a ferromagnetic intraatomic Hund's exchange J_H . In the context of the manganites, the DDEX model can be greatly simplified since J_H is much larger than the electronic bandwidth and the superexchange between core spins, which are treated as classical. In the limit $J_H \rightarrow \infty$, the itinerant-electron spins are perfectly aligned with the local-moment spins. Therefore the itinerant electrons can move only in a ferromagnetic background. The complex CE superstructure is the result of the frustration between the electronic kinetic energy and the antiferromagnetic superexchange between the core spins. In this phase, the electronic kinetic energy is directed along ferromagnetic zigzag chains that form because of a cooperative ordering of charge and orbital degrees of freedom.¹⁵

Although the DDEX model treated in the semiclassical approximation can explain the richness of the phase diagram¹⁴ and in particular account for the CE structure observed in the close vicinity of half filling,^{4,32,35,42} the calculation of the magnetic excitation spectra within the DDEX model is extremely difficult since it requires finite J_H and quantum-mechanical treatment of the core spins.^{43,44} To avoid these complications, we compute the spectrum from a spin-only model with effective exchange couplings that includes both AFM-super- and FM-double-exchange contributions. The latter are expected to contribute predominantly along the chains and to overcompensate the bare AFM superexchange. Consequently, a minimal effective model consists of FM couplings J_{FM} along the chains and AFM couplings J_{AFM} between the chains.

Indeed, the magnetic excitation spectrum of the layered system $\text{La}_{0.5}\text{Sr}_{1.5}\text{MnO}_4$ can be explained remarkably well by this minimal model.¹⁵ Including an additional next-nearest-neighbor exchange $J_{FM,2}$ between Mn^{4+} sites along the chains (Fig. 6) and a small single-ion anisotropy Λ to account for the spin gap, one finds an excellent description of the neutron-scattering data even for optical branches at higher energies, which has been interpreted as further evidence for

the existence of the AFM CE-type superstructure at half filling.

In the following, we use exactly the same model to fit the spectrum of the perovskite $\text{Nd}_{0.5}\text{Sr}_{0.5}\text{MnO}_3$ including an additional coupling $J_{AFM,c}$ along the c direction (Fig. 6). The effective spin-only Hamiltonian reads

$$\hat{H} = -J_{FM} \sum_{\langle i,j \rangle_{\parallel}} \hat{S}_i \hat{S}_j - J_{FM,2} \sum_{\langle\langle i,j \rangle\rangle_{\parallel}} \hat{S}_i \hat{S}_j + J_{AFM} \sum_{\langle i,j \rangle_{\perp}} \hat{S}_i \hat{S}_j + J_{AFM,c} \sum_{\langle i,j \rangle_c} \hat{S}_i \hat{S}_j + \Lambda \sum_i (\hat{S}_i^z)^2, \quad (1)$$

where the exchange couplings J_{FM} , $J_{FM,2}$, J_{AFM} , $J_{AFM,c}$ and single-ion anisotropy Λ are defined to be positive. The sites on the three-dimensional lattice are labeled by i , $\langle \cdot, \cdot \rangle_{\parallel}$ and $\langle\langle \cdot, \cdot \rangle\rangle_{\parallel}$ denote nearest- and next-nearest-neighbor bonds along the FM zigzag chains. Note that $J_{FM,2}$ acts only between Mn^{4+} spins on the corners of the chains. Nearest-neighbor

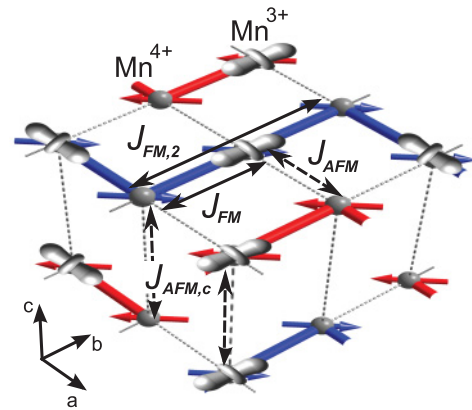


FIG. 6. (Color online) Illustration of the effective spin-only model for the AFM CE-type structure. Spins along the zigzag chains are coupled by ferromagnetic nearest- and next-nearest-neighbor exchanges J_{FM} and $J_{FM,2}$, the latter acting only between Mn^{4+} sites. The chains are coupled antiferromagnetically by exchanges J_{AFM} and $J_{AFM,c}$ between neighbors in the ab plane and along the c axis, respectively.

bonds between the chains in the ab plane and along the c direction are denoted by $\langle \cdot, \cdot \rangle_{\perp}$ and $\langle \cdot, \cdot \rangle_c$, respectively. In order to facilitate the comparison with Ref. 15 we use the same definition of the sum: each bond appears only once.

In the following, we use linear spin-wave theory to calculate the magnetic excitation spectrum and subsequently fit the experimental data. The procedure is standard and details can be found elsewhere.^{45,46} After representing the spins by Holstein-Primakoff bosons the spectrum is obtained by a Bogoliubov transformation, which amounts to diagonalizing a 16×16 matrix, which is explicitly given in Ref. 45 in the case $J_{FM,2} = \Lambda = 0$.

Whereas the idealized CE structure assumes a checkerboard ordering of Mn^{3+} and Mn^{4+} sites with corresponding local moment spins of $S_1 = 2$ and $S_2 = 3/2$, respectively, the experimentally observed charge and spin modulations are significantly smaller. To account for this, in the following we use $S_1 = 1.79$ and $S_2 = 1.67$ such that $S_1 S_2 = 3$ and $S_1/S_2 = 3/2.8$ equal to the ratio of the measured moments.^{32,35}

The best fit parameters are summarized in Table I. As in the layered system,¹⁵ the FM coupling along the chains J_{FM} is found to be much larger than the AFM in-plane coupling J_{AFM} between the chains. For the $\text{La}_{0.5}\text{Sr}_{1.5}\text{MnO}_4$ compound we used for the spins of Mn^{3+} $S_1 = 2$ and for the spins of Mn^{4+} $S_2 = 1.5$. As the product of $S_1 S_2 = 3$ is the same for both systems, the nearest-neighbor parameters J_{FM} and J_{AFM} can directly be compared.

This observation and the ratio $J_{AFM,c}/J_{AFM} \approx 4$ are in agreement with a quantitative estimate of the exchange couplings based on a modified Kanomori model, which carefully takes details of the lattice structures of various CE-type manganites into account.⁴⁷

$J_{AFM,c}$ connects either two Mn^{3+} or two Mn^{4+} sites, whereas J_{AFM} couples one Mn^{3+} and one Mn^{4+} site where imperfect orbital polarization will imply a FM double-exchange interaction rendering the AFM superexchange. As in addition the crystal lattice is considerably flattened, $J_{AFM,c}$ is much larger than J_{AFM} . In our model we include a simple single-ion anisotropy term $\Lambda \sum_i (\hat{S}_i^z)^2$. The ordered moments in the CE-type phase in $\text{Nd}_{0.5}\text{Sr}_{0.5}\text{MnO}_3$ are aligned along the ab plane. Therefore an anisotropy term perfectly accounts for an ab easy-plane system. However, the spins seem to be well fixed also within the ab layers causing a splitting in the zone-center magnon energies.²⁵ The same situation is also found in single-layered $\text{La}_{0.5}\text{Sr}_{1.5}\text{MnO}_4$, where the lower excitation could be assigned to the in-plane anisotropy. Also in $\text{Nd}_{0.5}\text{Sr}_{0.5}\text{MnO}_3$ we may identify the lower excitation with the in-plane anisotropy. It costs more energy to rotate the spins into

the c direction. A full treatment for such complex anisotropy has been given for a simple AFM layered structure in Ref. 48.

Inelastic neutron-scattering experiments have been able to determine the spin-wave excitations of $\text{Nd}_{0.5}\text{Sr}_{0.5}\text{MnO}_3$ for energies up to about 12 meV. Our data exhibit a steeper magnetic dispersion parallel to the zigzag chains while the dispersion perpendicular to the chains is flatter. This observation is in contrast to the Zener-polaron model, which implies a strong coupling inside the dimers. Taking this and the magnetic structure of the Zener-polaron scenario into account one obtains just the opposite anisotropy in the dispersion slopes along the Γ - B and Γ - C directions studied here. The spin-wave theory within the CE-type structure explains perfectly our experimental data. The experimental and the theoretical analysis are in agreement with the single-layered compound $\text{La}_{0.5}\text{Sr}_{1.5}\text{MnO}_4$.¹⁵ Consequently we may extend the strong support of the Goodenough model to perovskite manganites around half doping.

IV. FERROMAGNETIC METALLIC STATE IN $\text{Nd}_{0.50}\text{Sr}_{0.50}\text{MnO}_3$

In order to analyze the competition between the insulating COSO and the FMM phases in $\text{Nd}_{0.5}\text{Sr}_{0.5}\text{MnO}_3$ we performed studies of the magnon dispersion in the FMM phase as well. The magnetic excitations in the FMM state in perovskite manganites have been studied in many different compounds and a damping of the spin-wave dispersion toward the zone boundaries have been reported in many cases.^{24,26,29–31,49,50} To explain this behavior, several microscopic mechanisms have been proposed, without reaching a clear conclusion (for a brief summary, see Ref. 51). One explanation for the softening of the spin-wave dispersion might be the development of quantized spin waves within ferromagnetic clusters of restricted sizes as reported in Refs. 27 and 31.

We studied the spin dynamics of $\text{Nd}_{0.5}\text{Sr}_{0.5}\text{MnO}_3$ at $T = 174$ K, where the ferromagnetic signal of the reflection at $\mathbf{Q}_{FM} = (1,0,0)$ exhibits its maximum [see Fig. 2(e)]. To investigate magnetic excitations along the main-symmetry directions $[1,0,0]$, $[0,1,1]$, and $[1,1,1]$, we aligned the sample with reflections $(1,0,0)$ and $(0,1,1)$ defining the scattering plane. All data have been collected around the Bragg reflections $\mathbf{Q}_{FM} = (1,0,0)$, $\mathbf{Q}_{FM} = (0,1,1)$, and $\mathbf{Q}_{FM} = (1,1,1)$. Most data have been collected with the thermal spectrometer 1T with fixed $E_f = 14.7$ meV. The calibration of the spectrometer has been checked by a vanadium standard crystal. An energy scan with $E_f = 14.7$ meV indicates a resolution of $\Delta E \approx 1$ meV. Figure 7 presents the spin-wave dispersion along the main symmetry directions. The data have been corrected by the Bose factor and finally fitted with the RESLIB code, which calculates the convolution of the four-dimensional resolution function with the dispersion.⁵² We were able to investigate magnetic excitations of the acoustic branch along the Γ - R , Γ - M , and Γ - X paths. An energy scan with the cold-source spectrometer 4F.2 at the zone center $\mathbf{Q}_{FM} = (1,0,0)$ yields no evidence for an excitation gap. Constant-energy scans around the ferromagnetic zone-center $\mathbf{Q}_{FM} = (1,0,0)$ are depicted in Fig. 8(a). Investigations in different Brillouin zones clearly identify a magnetic origin for the signals appearing at low-energy transfer, since the intensity follows the magnetic

TABLE I. Results of the obtained fit parameters in the AFM CE-type state for $\text{Nd}_{0.5}\text{Sr}_{0.5}\text{MnO}_3$ in comparison to the fit parameters in $\text{La}_{0.5}\text{Sr}_{1.5}\text{MnO}_4$ from Ref. 15.

	$\text{Nd}_{0.5}\text{Sr}_{0.5}\text{MnO}_3$	$\text{La}_{0.5}\text{Sr}_{1.5}\text{MnO}_4$
J_{FM} (meV)	6.76	9.98
$J_{FM,2}$ (meV)	2.76	1.83
J_{AFM} (meV)	0.75	3.69
$J_{AFM,c}$ (meV)	3.22	

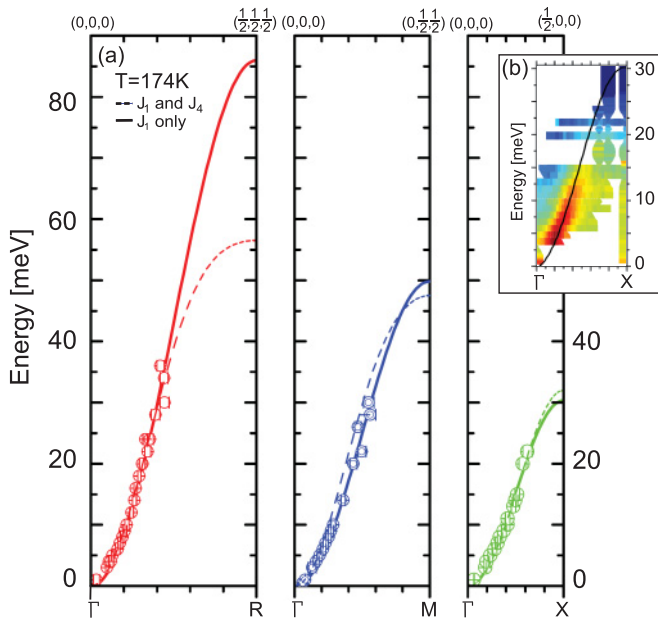


FIG. 7. (Color online) Full spin-wave dispersion along the main-symmetry directions in the FMM state in $\text{Nd}_{0.5}\text{Sr}_{0.5}\text{MnO}_3$ at $T = 174$ K. Experimental data were taken along the Γ -R, Γ -M, and Γ -X directions, respectively. Solid lines refer to a fit with a Heisenberg ferromagnet with only nearest-neighbor interactions and dotted lines to a fit with nearest- and forth-nearest-neighbor interactions. A significant improvement of the fit to the data by taking additionally J_4 into account cannot be observed. An enhanced signal around the zone boundary might be given by several magnetic levels (b). For more details see text.

form factor as shown in Fig. 8(b). In Ref. 25 the spin-wave dispersion in the FMM state in $\text{Nd}_{0.5}\text{Sr}_{0.5}\text{MnO}_3$ along different symmetry directions has been studied and an extremely flat dispersion with energies around 10 meV at the zone boundaries is reported. Our experiments disagree with these observations since our data yield much steeper branches. For example, clear excitations along the $[1,1,1]$ direction between energies of $E = 18$ meV and $E = 22$ meV can be observed in the middle of the

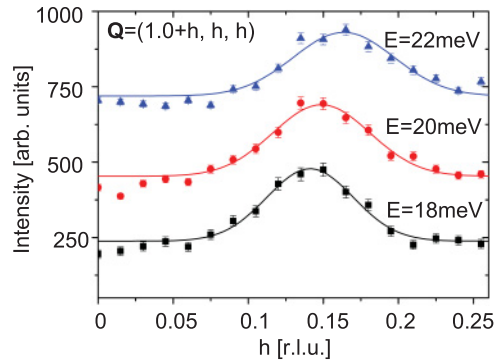


FIG. 9. (Color online) Observed excitation at high energies along the symmetry direction $[1,1,1]$. The maximum shifts to increasing q with increasing energy indicating the steeper dispersion.

Brillouin zone (see Fig. 9). The main magnetic signal seems to stem from the simple ferromagnetic magnon branch; but there are weak but significant additional signals that are most likely magnetic as well. The constant energy cuts $(h,0,0)$ across the $(1,0,0)$ FM Bragg peak show more intensity near the magnetic zone boundaries $\approx(0.5,0,0)$ than at the center, which cannot be attributed to the background. Also the energy scan at $(1.5,0,0)$ exhibits significant intensity below the energy of the magnon branch [Fig. 7(b)]. This scattering resembles the splitting of the magnon branches observed in $\text{La}_{1-x}(\text{Ca,Sr})_x\text{MnO}_3$ at lower doping, which was attributed to a confinement.^{27,31} However, such confinement effect—if present—must be much weaker in this higher-doped $\text{Nd}_{0.5}\text{Sr}_{0.5}\text{MnO}_3$ material.

Spin-wave dispersion in 113 manganites with a large electron bandwidth and high T_C can be described by calculations with the conventional Heisenberg model including only the nearest-neighbor exchange interactions.^{49,53} In the following the description our data takes only the sharp signals into account without keeping the increasing intensity near the zone boundaries in mind. To evaluate the spin-wave dispersion in $\text{Nd}_{0.5}\text{Sr}_{0.5}\text{MnO}_3$ we use two models: (i) we consider only the ferromagnetic coupling between nearest-neighbor interaction J_1 , (ii) nearest-neighbor interactions J_1 and fourth-nearest interactions J_4 are taken into account.

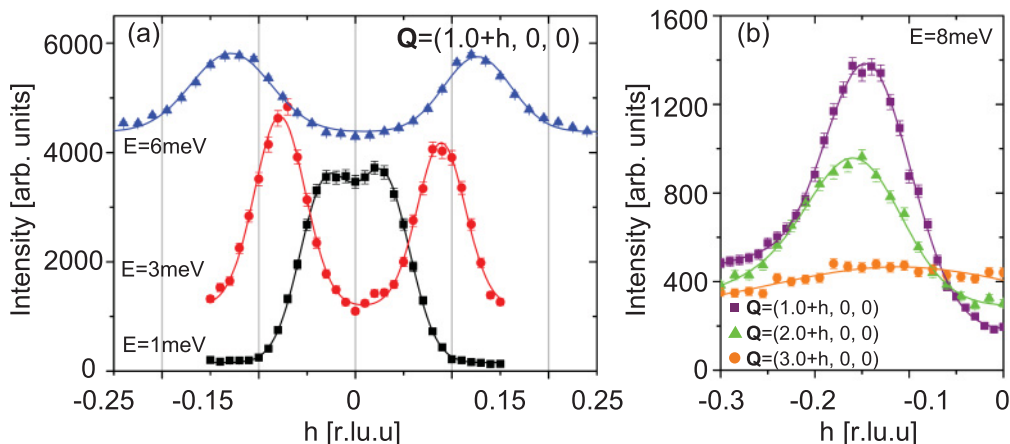


FIG. 8. (Color online) Constant-energy scans around the zone center $\mathbf{Q}_{FM} = (1,0,0)$ in $\text{Nd}_{0.5}\text{Sr}_{0.5}\text{MnO}_3$ along the symmetry direction $[1,0,0]$. Data at $E = 1$ and 3 meV are recorded with the spectrometer 1T with fixed $E_f = 8.05$ meV and at $E = 8$ meV with fixed $E_f = 14.7$ meV, respectively (a). A decrease of the signal with increasing scattering vector demonstrates its magnetic origin (b).

The Hamiltonian of a Heisenberg ferromagnet can be written as

$$\hat{H} = - \sum_{ij} J_{ij} \mathbf{S}_i \mathbf{S}_j \quad (2)$$

Hereby J_{ij} describes the magnetic exchange coupling between two spins \mathbf{S}_i and \mathbf{S}_j at the position \mathbf{R}_i and \mathbf{R}_j . Note that a pair appears twice in the sum.⁵⁴ In linear approximation the spin-wave dispersion with only ferromagnetic coupling ($J_{ij} > 0$) becomes

$$E(\mathbf{q}) = \hbar\omega(\mathbf{q}) = \Delta + 2S[J(\mathbf{0}) - J(\mathbf{q})] \quad (3)$$

with

$$J(\mathbf{q}) = \sum_j J_{ij} e^{i\mathbf{q}(\mathbf{R}_i - \mathbf{R}_j)}.$$

A finite-energy gap near the zone center can be controlled by Δ . Since we do not observe a finite gap for the $[1,0,0]$, $[0,1,1]$, and $[1,1,1]$ directions, we will set Δ equal to zero.

The simplest case with only nearest-neighbor J_1 interactions leads to the relation

$$E(\mathbf{q}) = \Delta + 4SJ_1[3 - \cos(q_h a) - \cos(q_k a) - \cos(q_l a)]. \quad (4)$$

Taking only J_1 into account, we can very well describe our experimental data (Fig. 7, solid lines). The fits of the data with only the nearest-neighbor interaction J_1 yield $2SJ_1 = 7.6(2)$ meV for the $[1,0,0]$, $2SJ_1 = 6.3(2)$ meV for the $[0,1,1]$, and $2SJ_1 = 7.2(2)$ meV for the $[1,1,1]$ directions. To compare an improvement of the description of the fit by introducing the coupling J_4 as suggested previously in Ref. 50, the dispersion for the $[1,0,0]$ direction takes the form [Fig. 11(b)]

$$E(\mathbf{q}) = \Delta + 4SJ_1 \{ [1 - \cos(2\pi q_h)] \} + 4SJ_4 \{ [1 - \cos(4\pi q_h)] \}. \quad (5)$$

The best fit to the data with nearest-neighbor and fourth-nearest interaction is depicted in Fig. 7 by the dotted lines. There is only little difference in the spin-wave dispersion of the two models in the energy range studied. Therefore our data give no support for a related $2SJ_4$ parameter.

In the CE-type state we obtained the best fit to the data for the ferromagnetic coupling parallel to the chains with $2SJ_{FM} = 11.7$ meV. In the FM state we can describe the data with a mean exchange energy of $2SJ_1 = 7.0(5)$ meV for the fit with nearest-neighbor interaction taken into account. This means the nearest-neighbor ferromagnetic exchange in the FM state is strongly reduced by a factor of about 1.5 in comparison to the AFM CE-type state, but note that each spin has six ferromagnetically coupled spins in the FMM state, compared to only two FM neighbors in the CE phases. In the single-layered compounds $\text{La}_{0.5}\text{Sr}_{1.5}\text{MnO}_4$ an exchange energy of $2SJ_{FM} = 7.5(5)$ meV has been observed above the AFM CE-type ordered state.¹⁹ Consequently, the exchange parameters in the FM states in $\text{La}_{0.5}\text{Sr}_{1.5}\text{MnO}_4$ and in $\text{Nd}_{0.5}\text{Sr}_{0.5}\text{MnO}_3$ are almost identical. This result is quite interesting since the single-layered compound does not show metallic behavior and possesses fewer neighbors. More importantly, the layered compound only exhibits ferromagnetic fluctuations generated by ferromagnetic clusters with finite size above T_{CO} . Our investigation in the FMM state in $\text{Nd}_{0.5}\text{Sr}_{0.5}\text{MnO}_3$ indicates

a quite good description of the data along the main-symmetry directions by taking only the nearest-neighbor coupling J_1 into account (but note that our model is slightly oversimplified since we do not take the intensities near the zone boundary into account).

To get a more precise perception of the magnetic excitation in the FMM state in $\text{Nd}_{1-x}\text{Sr}_x\text{MnO}_3$ and to compare the exchange parameters we decided to study the spin-wave dispersion in a slightly electron-doped single crystal with a composition of $\text{Nd}_{0.51}\text{Sr}_{0.49}\text{MnO}_3$.

V. FERROMAGNETIC METALLIC STATE IN $\text{Nd}_{0.51}\text{Sr}_{0.49}\text{MnO}_3$

A single crystal of $\text{Nd}_{1-x}\text{Sr}_x\text{MnO}_3$ with doping level $x = 0.49$ has been characterized by temperature-dependent measurements of magnetization, resistivity, x-ray, neutron diffraction, and energy-dispersive x-ray (EDX) analysis. A significant drop of resistivity accompanied by an increase of magnetization reminiscent of the FMM state is observed at $T_C \approx 245$ K (Fig. 10). In accordance with the macroscopic studies, the scattering at $\mathbf{Q}_{FM} = (1,1,0)$ exhibits an increase of intensity below T_C , which can be ascribed to ferromagnetic correlations [Fig. 10(c)]. Upon further cooling, the electric resistivity increases by more than two orders of magnitude at the first-order transition into the COSO state at $T_{CO} \approx 112$ K. Temperature-dependent investigations of the superstructure reflection referring to orbital ordering $\mathbf{Q}_{OO} = (2.25, 0.25, 0)$ yield a sizable signal below T_{CO} [Fig. 10(d)]. Comparing the transition temperatures into the COSO state in $\text{Nd}_{1-x}\text{Sr}_x\text{MnO}_3$ for $x = 0.50$ and $x = 0.49$, we observe a less robust COSO state in $\text{Nd}_{0.51}\text{Sr}_{0.49}\text{MnO}_3$. Before discussing inelastic data we want to compare the ground-state properties of the ideally doped system ($x = 0.5$) in comparison to the slightly electron-doped system ($x = 0.49$). In $\text{Nd}_{0.51}\text{Sr}_{0.49}\text{MnO}_3$ below $T \approx 50$ K, the electric resistivity is almost constant. In contrast, for $x = 0.5$ we find a continuous increase of resistivity below T_{CO} up to $\rho \approx 10^4$ Ω m at the lowest temperature in comparison to $\rho \approx 10^0$ Ω m for $x = 0.49$. The slight doping difference between these two compounds strongly affects the magnetization at low temperatures as well. The magnetization with an applied field of $B = 50$ mT saturates with $m = 0.05\mu_B/\text{Mn}$ for $x = 0.49$ while the magnetization for $x = 0.50$ tends to zero at low temperatures. These properties underline the coexistence of antiferromagnetic CE-type and ferromagnetic ordering in the ground state of $\text{Nd}_{0.51}\text{Sr}_{0.49}\text{MnO}_3$ as reported in Ref. 32. Neutron diffraction of the reflection $\mathbf{Q}_{FM} = (1,1,0)$ further supports this interpretation. The signal below T_C increases as in the half doped system, but in the COSO state in $x = 0.49$ a high intensity can still be recorded at low temperature. We analyzed the stoichiometry of the samples with EDX analysis. However, the accuracy of this method does not allow for determining the content of oxygen concentration. Hence we may not rule out an oxygen deficiency. Concerning the various transition temperatures and the temperature dependence of the electrical resistivity our sample is fully comparable to the $\text{Nd}_{0.51}\text{Sr}_{0.49}\text{MnO}_3$ crystal studied in Ref. 32.

We have studied the spin-wave excitations in $\text{Nd}_{0.51}\text{Sr}_{0.49}\text{MnO}_3$ at $T = 151$ K, which is well in the

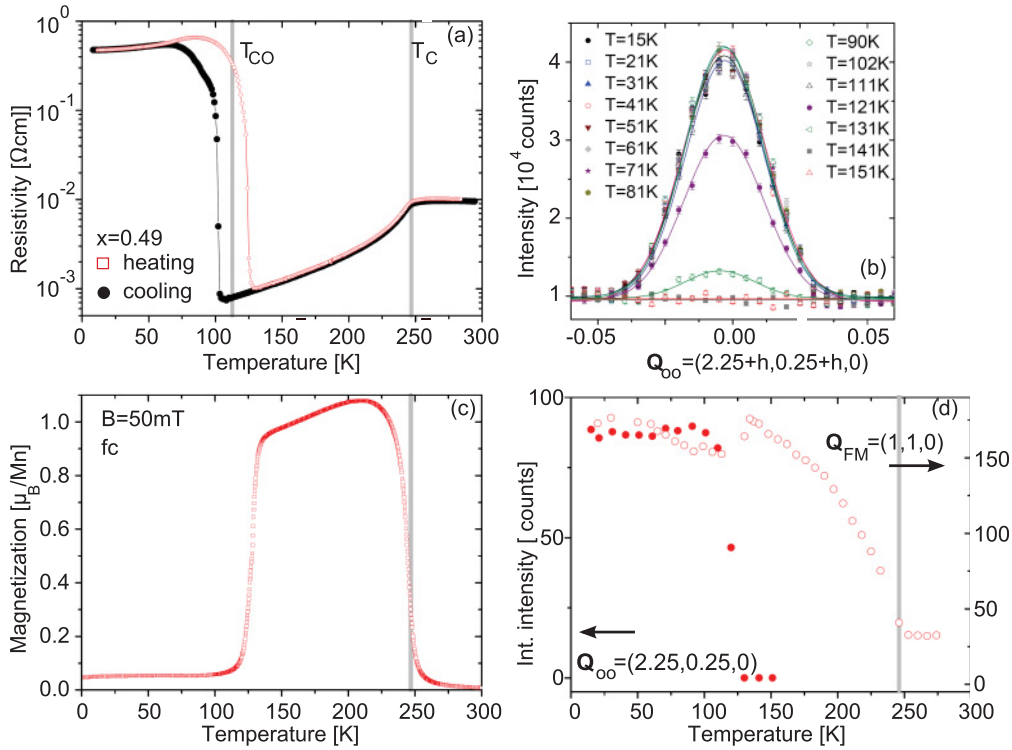


FIG. 10. (Color online) Characterization of the single crystal $\text{Nd}_{0.51}\text{Sr}_{0.49}\text{MnO}_3$ by macroscopic and microscopic studies. A ferromagnetic metallic state can be observed by electric resistivity measurements and magnetization data (a),(c). Elastic neutron scattering at $\mathbf{Q}_{FM} = (1,1,0)$ confirms ferromagnetic ordering below T_C (d). A sudden increase in intensity of the superstructure reflection $\mathbf{Q}_{OO} = (2.25,0.25,0)$ below T_{CO} refers to orbital ordering (b),(d).

ferromagnetically ordered state, and present an analysis of the data with the same Heisenberg models as those used for the half doped compound. The scattering experiments have been performed by aligning the crystal with the reflections $(1,0,0)/(0,1,1)$, allowing momentum transfers of the kind (h,l,l) . We focused our measurement on excitations along the symmetry directions $[1,0,0]$ and $[0,1,1]$ in cubic notation. Data have been measured in the Brillouin zones around the zone centers $\mathbf{Q}_{FM} = (1,0,0)$ and $\mathbf{Q}_{FM} = (0,1,1)$ and were finally combined. The data have been corrected by the Bose factor and finally fitted with the convolution of the four-dimensional resolution function with the dispersion. Fits to the data result in the spin-wave dispersion as shown in Fig. 11. Raw-data scans with fixed energy around ferromagnetic zone centers along the $[1,0,0]$ and $[0,1,1]$ directions are depicted Fig. 12.

In the following we will prove the experimental data of the sharp signals with the Heisenberg model as described for the half doped system. The investigations of the dispersion near the zone center Γ with the cold triple-axis spectrometer are in agreement with our observations in $\text{Nd}_{0.5}\text{Sr}_{0.5}\text{MnO}_3$ and we find no indication for a spin-wave gap in $\text{Nd}_{0.51}\text{Sr}_{0.49}\text{MnO}_3$. Consequently, we set Δ equal to zero in our calculation. To evaluate the spin-wave dispersion in $\text{Nd}_{0.51}\text{Sr}_{0.49}\text{MnO}_3$ we make the same assumptions as those used for the $x = 0.5$ compound: (i) we consider only the ferromagnetic coupling between nearest-neighbor interaction J_1 , and (ii) nearest-neighbor interactions J_1 and fourth-nearest interactions J_4 are taken into account.

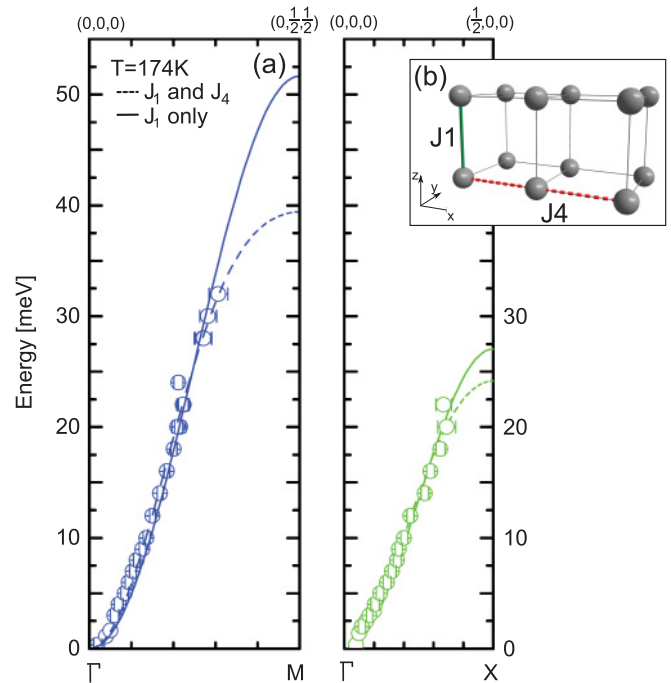


FIG. 11. (Color online) Dispersion of the magnon excitation in the FMM state in $\text{Nd}_{0.51}\text{Sr}_{0.49}\text{MnO}_3$ along the symmetry directions $[1,0,0]$ and $[0,1,1]$ at $T = 151$ K (a). Solid lines refer to fits with only nearest-neighbor interactions J_1 and dashed lines point to calculations with nearest and fourth-nearest-neighbor interactions J_1 and J_4 as depicted in (b).

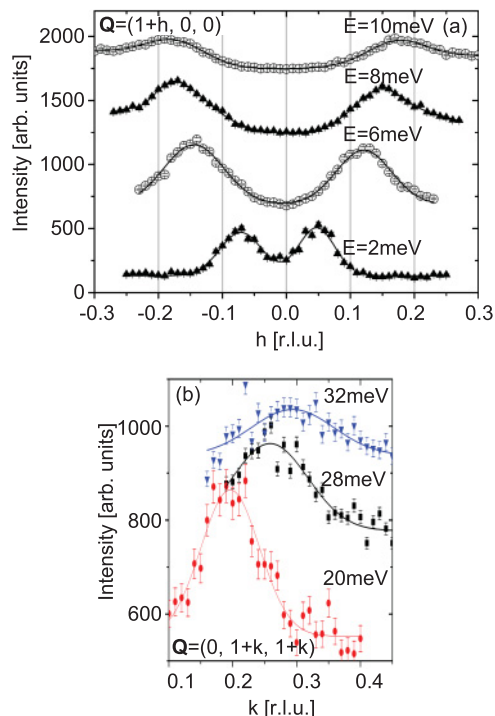


FIG. 12. (Color online) Raw-data scans with fixed energy observed in $[1,0,0]$ direction. Data at 2 meV are taken with $E_f = 8.05$ meV and above with $E_f = 14.7$ meV. Intensities are normalized to the same monitor but shifted as a guide to the eyes (a). Signals along the symmetry direction $[0, 1, 1]$ exhibit a loss in intensity and an increase of width with increasing energy, too (b).

All fit parameters for the spin-wave dispersion in $\text{Nd}_{0.51}\text{Sr}_{0.49}\text{MnO}_3$ and $\text{Nd}_{0.5}\text{Sr}_{0.5}\text{MnO}_3$ are summarized in Table II. Since no significant improvement of the reduced χ -squared χ_{red}^2 for the model including J_4 and since the ratio of J_4/J_1 is quite small, there is no evidence that the fourth-nearest neighbors is needed to describe the ferromagnetic spin-wave dispersion in $\text{Nd}_{1-x}\text{Sr}_x\text{MnO}_3$ with $x = 0.49$.

Our studies for $x = 0.49$ yield the identical dispersion in comparison to the optimal-doped compound $x = 0.5$ in the FMM state. Near the zone center the signal is sharp and resolution limited. One can easily notice that the intensity with increasing energy shrinks and the width starts to increase. Following the sharp excitations with increasing energy, toward the zone boundary the signal is hampered, similar to observations in the optimal doped compound $x = 0.50$.

The observation of nearly identical exchange parameters in $\text{Nd}_{1-x}\text{Sr}_x\text{MnO}_3$ with $x = 0.49$ and $x = 0.50$ again emphasizes an identical FMM state in $x = 0.49$ and $x = 0.50$. The FMM state in $\text{Nd}_{1-x}\text{Sr}_x\text{MnO}_3$ seems to be less sensitive to the doping than the COSO phase, which is severely damaged by the small amount of holes in $\text{Nd}_{0.51}\text{Sr}_{0.49}\text{MnO}_3$.

VI. SUMMARY

In conclusion, we have studied the microscopic origin of the COSO state in $\text{Nd}_{0.5}\text{Sr}_{0.5}\text{MnO}_3$ and the FMM state

TABLE II. Fit parameters for the spin-wave dispersion in $\text{Nd}_{1-x}\text{Sr}_x\text{MnO}_3$ with $x = 0.49$ and $x = 0.50$ in the FMM state. The data have been obtained from two different models. In model 1, only nearest-neighbor interactions J_1 and model 2, nearest-neighbor interactions J_1 , and fourth-nearest interactions J_4 are taken into account.

	$\text{Nd}_{0.51}\text{Sr}_{0.49}\text{MnO}_3$		$\text{Nd}_{0.5}\text{Sr}_{0.5}\text{MnO}_3$			
	$[1,0,0]$	$[0,1,1]$	$[1,0,0]$	$[0,1,1]$	$[1,1,1]$	
Model 1						
$2SJ_1$ (meV)	2.8	6.8(3)	6.5(3)	7.6(2)	6.3(2)	7.2(2)
Model 2						
$2SJ_1$ (meV)	6.0(3)	4.9(2)	8.0(3)	5.3(9)	2.1(9)	
$2SJ_4$ (meV)	0.5(2)	0.8(1)	-0.2(2)	0.4(4)	0.4(3)	
J_4/J_1 (%)	8	16	2	8	19	

in $\text{Nd}_{1-x}\text{Sr}_x\text{MnO}_3$ with $x = 0.50$ and $x = 0.49$ by inelastic neutron scattering. Despite the complications arising from the twinning in these perovskite manganites with pseudocubic structure, we were able to observe excitations along the main-symmetry directions up to $E \approx 12$ meV in the AFM ground state of $x = 0.5$. We clearly find an anisotropic dispersion between the directions parallel and perpendicular to the orbital zigzag chains. Theoretical descriptions of the spin-wave dispersion by the AFM CE-type ordering perfectly describe our experimental data yielding results similar to the single-layered compound $\text{La}_{0.5}\text{Sr}_{1.5}\text{MnO}_4$.¹⁵ The good description of the experimental dispersion gives strong support for the qualitative CE-type Goodenough model. A model with bond-centered charge order is even unable to explain the sign of the anisotropy. Although the Zener-polaron picture cannot explain the data, a superposition of both the Goodenough model and the Zener polaron as suggested in Ref. 14 cannot fully be excluded. The stacking of magnetic order along the c direction, i.e., perpendicular to the planes of the zigzag chains, is rather strong. This finding can be understood by the flattening of the crystal structure and by the fact this stacking arises from strong $\text{Mn}^{3+}\text{-Mn}^{3+}$ and $\text{Mn}^{4+}\text{-Mn}^{4+}$ interactions.

The FMM state has been investigated in the half doped compound $\text{Nd}_{0.5}\text{Sr}_{0.5}\text{MnO}_3$ and in the slightly electron-doped system $\text{Nd}_{0.51}\text{Sr}_{0.49}\text{MnO}_3$. Both concentrations exhibit nearly the same spin-wave spectra, proving that the FMM state is little affected by the slight difference in doping. In $\text{Nd}_{0.5}\text{Sr}_{0.5}\text{MnO}_3$ the magnon dispersion along the main symmetry directions $[1,0,0]$, $[0,1,1]$, and $[1,1,1]$ can be observed. The FMM state seems to consist of two parts; (i) a spin-wave dispersion, which can be easily described with a Heisenberg model taking only nearest-neighbors interactions into account, and (ii) weak additional intensities near the zone boundaries over a wide energy band. The spin-wave dispersion in $\text{Nd}_{0.51}\text{Sr}_{0.49}\text{MnO}_3$ along the $[1,0,0]$ and $[0,1,1]$ directions exhibits identical results with a steep dispersion and damped excitations near the zone boundary.

ACKNOWLEDGMENTS

This work was supported by the Deutsche Forschungsgemeinschaft through the Sonderforschungsbereich 608. We

thank S. Heijligen for the SQUID measurements. F.K. acknowledges financial support from EPSRC under Grant No. EP/I004831/1. A.N. thanks Cologne University and SFB 608 for hospitality.

*ulbrich@ph2.uni-koeln.de

†frank.kruger@st-andrews.ac.uk

‡braden@ph2.uni-koeln.de

¹G. H. Jonker and J. H. V. Santen, *Physica* **16**, 337 (1950).

²J. H. V. Santen and G. H. Jonker, *Physica* **16**, 599 (1950).

³Y. Tokura and Y. Tomioka, *J. Magn. Mater.* **200**, 1 (1999).

⁴P. G. Radaelli, D. E. Cox, M. Marezio, and S.-W. Cheong, *Phys. Rev. B* **55**, 3015 (1997).

⁵H. Kawano, R. Kajimoto, H. Yoshizawa, J. A. Fernandez-Baca, Y. Tomioka, H. Kuwahara, and Y. Tokura, *Physica B: Condensed Matter* **241**, 289 (1997).

⁶J. van den Brink, G. Khaliullin, and D. Khomskii, *Phys. Rev. Lett.* **83**, 5118 (1999).

⁷S. Yunoki, T. Hotta, and E. Dagotto, *Phys. Rev. Lett.* **84**, 3714 (2000).

⁸R. Kajimoto, H. Yoshizawa, Y. Tomioka, and Y. Tokura, *Phys. Rev. B* **66**, 180402 (2002).

⁹E. O. Wollan and W. C. Koehler, *Phys. Rev.* **100**, 545 (1955).

¹⁰J. Goodenough, *Phys. Rev.* **100**, 564 (1955).

¹¹Z. Jirák, F. Damay, M. Hervieu, C. Martin, B. Raveau, G. André, and F. Bourée, *Phys. Rev. B* **61**, 1181 (2000).

¹²J. Herrero-Martín, J. García, G. Subías, J. Blasco, and M. C. Sánchez, *Phys. Rev. B* **70**, 024408 (2004).

¹³A. Doud-Aladine, J. Rodríguez-Carvajal, L. Pinsard-Gaudart, M. Fernandez-Diaz, and A. Revcolevschi, *Phys. Rev. Lett.* **89**, 097205 (2002).

¹⁴D. Efremov, J. van den Brink, and D. Khomskii, *Nat. Mater.* **3**, 853 (2004).

¹⁵D. Senff, F. Krüger, S. Scheidl, M. Benomar, Y. Sidis, F. Demmel, and M. Braden, *Phys. Rev. Lett.* **96**, 257201 (2006).

¹⁶G. Jung, V. Markovich, C. J. van der Beek, D. Mogilyansky, and Y. M. Mukovskii, *Phys. Rev. B* **72**, 134412 (2005).

¹⁷P. Reutler, O. Friedt, B. Büchner, M. Braden, and A. Revcolevschi, *J. Cryst. Growth* **249**, 222 (2003).

¹⁸D. Senff, P. Reutler, M. Braden, O. Friedt, D. Bruns, A. Cousson, F. Bourée, M. Merz, B. Büchner, and A. Revcolevschi, *Phys. Rev. B* **71**, 024425 (2005).

¹⁹D. Senff, O. Schumann, M. Benomar, M. Kriener, T. Lorenz, Y. Sidis, K. Habicht, P. Link, and M. Braden, *Phys. Rev. B* **77**, 184413 (2008).

²⁰H. Ulbrich, D. Senff, P. Steffens, O. J. Schumann, Y. Sidis, P. Reutler, A. Revcolevschi, and M. Braden, *Phys. Rev. Lett.* **106**, 157201 (2011).

²¹Y. Tokura and N. Nagaosa, *Science* **288**, 462 (2000).

²²M. Tokunaga, N. Miura, Y. Moritoma, and Y. Tokura, *Phys. Rev. B* **59**, 11151 (1999).

²³H. Yoshizawa, H. Kawano, J. Fernandez-Baca, H. Kuwahara, and Y. Tokura, *Phys. Rev. B* **58** (1998).

²⁴J. A. Fernandez-Baca, P. Dai, H. Y. Hwang, C. Kloc, and S.-W. Cheong, *Phys. Rev. Lett.* **80**, 4012 (1998).

²⁵H. Kawano-Furukawa, R. Kajimoto, H. Yoshizawa, Y. Tomioka, H. Kuwahara, and Y. Tokura, *Phys. Rev. B* **67**, 174422 (2003).

²⁶Y. Endoh, H. Hiraka, Y. Tomioka, Y. Tokura, N. Nagaosa, and T. Fujiwara, *Phys. Rev. Lett.* **94**, 017206 (2005).

²⁷M. Hennion, F. Moussa, P. Lehouelleur, F. Wang, A. Ivanov, Y. M. Mukovskii, and D. Shulyatev, *Phys. Rev. Lett.* **94**, 057006 (2005).

²⁸B. Kirby, J. Rhyne, H. Kaiser, H. Kuwahara, and Y. Tokura, *J. Magn. Mater.* **302**, 237 (2006).

²⁹F. Ye, P. Dai, J. A. Fernandez-Baca, H. Sha, J. W. Lynn, H. Kawano-Furukawa, Y. Tomioka, Y. Tokura, and J. Zhang, *Phys. Rev. Lett.* **96**, 047204 (2006).

³⁰F. Ye, P. Dai, J. A. Fernandez-Baca, D. T. Adroja, T. G. Perring, Y. Tomioka, and Y. Tokura, *Phys. Rev. B* **75**, 144408 (2007).

³¹S. Petit, M. Hennion, F. Moussa, D. Lamago, A. Ivanov, Y. M. Mukovskii, and D. Shulyatev, *Phys. Rev. Lett.* **102**, 207201 (2009).

³²R. Kajimoto, H. Yoshizawa, H. Kawano, H. Kuwahara, Y. Tokura, K. Ohoyama, and M. Ohashi, *Phys. Rev. B* **60**, 9506 (1999).

³³Y. Tokura, *Rep. Prog. Phys.* **69**, 797 (2006).

³⁴H. Kuwahara, Y. Tomioka, A. Asamitsu, Y. Moritomo, and Y. Tokura, *Science* **270**, 961 (1995).

³⁵H. Kawano, R. Kajimoto, H. Yoshizawa, Y. Tomioka, H. Kuwahara, and Y. Tokura, *Phys. Rev. Lett.* **78**, 4253 (1997).

³⁶J. Rodríguez-Carvajal, *Physica B* **192**, 55 (1993).

³⁷In the space group *Imma* it would align along the orthorhombic *b* direction.

³⁸D. Petitgrand, H. Casalta, P. Bourges, and A. S. Ivanov, *Physica B: Condensed Matter* **234**, 806 (1997).

³⁹V. V. Krishnamurthy, J. L. Robertson, R. S. Fishman, M. D. Lumsden, and J. F. Mitchell, *Phys. Rev. B* **73**, 060404 (2006).

⁴⁰L. F. Feiner and A. M. Oles, *Phys. Rev. B* **59**, 3295 (1999).

⁴¹T. Hotta, S. Yunoki, M. Mayr, and E. Dagotto, *Phys. Rev. B* **60**, R15009 (1999).

⁴²B. J. Sternlieb, J. P. Hill, U. C. Wildgruber, G. M. Luke, B. Nachumi, Y. Moritomo, and Y. Tokura, *Phys. Rev. Lett.* **76**, 2169 (1996).

⁴³N. Shannon and A. V. Chubukov, *Phys. Rev. B* **65**, 104418 (2002).

⁴⁴W. Lv, F. Krüger, and P. Phillips, *Phys. Rev. B* **82**, 045125 (2010).

⁴⁵C. I. Ventura and B. Alascio, *Phys. Rev. B* **68**, R020404 (2003).

⁴⁶O. Sikora and A. M. Oleś, *Physica B* **359–361**, 1300 (2005).

⁴⁷L. E. Gontchar and A. E. Nikiforov, *Phys. Rev. B* **66**, 014437 (2002).

⁴⁸L. Jongh, *Magnetic Properties of Layered Transition Metal Compounds* (Kluwer Academic, Dordrecht, 1990).

⁴⁹T. G. Perring, G. Aeppli, S. M. Hayden, S. A. Carter, J. P. Remeika, and S.-W. Cheong, *Phys. Rev. Lett.* **77**, 711 (1996).

⁵⁰H. Y. Hwang, P. Dai, S.-W. Cheong, G. Aeppli, D. A. Tennant, and H. A. Mook, *Phys. Rev. Lett.* **80**, 1316 (1998).

⁵¹J. Zhang, F. Ye, H. Sha, P. Dai, J. A. Fernandez-Baca, and E. W. Plummer, *J. Phys.: Condens. Matter* **19**, 315204 (2007).

⁵²A. Zheludev, *ResLib 3.3* (Oak Ridge National Laboratory, Oak Ridge, 2006).

⁵³M. C. Martin, G. Shirane, Y. Endoh, K. Hirota, Y. Moritomo, and Y. Tokura, *Phys. Rev. B* **53**, 14285 (1996).

⁵⁴In order to compare the *J*'s in the FMM state with those in the CE-type phase one needs to divide the latter by a factor of 2.